



Title	Interannual variations in the Hawaiian Lee Countercurrent
Author(s)	Abe, Hiroto; Hanawa, Kimio; Ebuchi, Naoto
Citation	Journal of Oceanography, 69(2), 191-202 https://doi.org/10.1007/s10872-012-0166-0
Issue Date	2013-04
Doc URL	http://hdl.handle.net/2115/57820
Rights	The final publication is available at link.springer.com
Type	article (author version)
File Information	JoO69-2 191-202.pdf



[Instructions for use](#)

1
2
3 **Interannual variations in the Hawaiian Lee Countercurrent**
4

5 Hiroto Abe^{1, 2}, Kimio Hanawa¹ and Naoto Ebuchi²
6
7
8
9
10

- 11 1. Department of Geophysics, Graduate School of Science, Tohoku University, 6-3,
12 Aramaki-Aza-Aoba, Aoba-ku, Sendai 980-8578, Japan
13 2. Institute of Low Temperature Science, Hokkaido University, Kita-19, Nishi-8,
14 Kita-ku, Sapporo 060-0819, Japan
15
16
17
18
19
20

21 Email: abe@lowtem.hokudai.ac.jp
22
23
24

June 27, 2012

Abstract

The Hawaiian Lee Countercurrent (HLCC) is an eastward surface current flowing against the broad westward flow of the North Pacific subtropical circulation. Analyses of satellite altimeter data over 16 years revealed that the HLCC is characterized by strong interannual variations. The strength and meridional location of the HLCC axis varied significantly year by year. The eastward velocity of the HLCC was higher when the location of the axis was stable. Mechanisms for the interannual variations were explored by analyses of the altimeter data and results from a simple baroclinic model. The interannual variations in the strength of the HLCC did not correlate with those of the wind stress curl (WSC) dipole formed on the leeward side of the Hawaii Islands, although the WSC dipole has been recognized as the generation mechanism of the HLCC. Meridional gradients of the sea surface height anomaly (SSHA) across the HLCC generated by baroclinic Rossby waves propagating westward from the east of the Hawaii Islands were suggested as a possible mechanism for the interannual variations in the HLCC. The spatial patterns in the observed SSHAs were reproduced by a linear baroclinic Rossby wave model forced by wind fields from a numerical weather prediction model. Further analysis of the wind data suggested that positive and negative anomalies of WSC associated with changes in the trade winds in the area east of the Hawaii Islands are a major forcing for generating SSHAs that lead to the HLCC variations with a time lag of about one year.

1. Introduction

The Hawaiian Lee Countercurrent (HLCC) is an eastward current located at the west of the Hawaii Islands. This narrow surface current flows against the North Equatorial Current (NEC) in the southern part of the subtropical gyre. Qiu et al. (1997) and Flament et al. (1998) discovered the HLCC by analyzing drifter data.

Recent intense observations of marine surface wind fields by spaceborne sensors revealed the existence of a number of wakes behind the individual islands, which are formed by impinging of the northeasterly trades on the islands (Xie et al., 2001). The individual wakes dissipate within a few hundred kilometers, and a broad wake is formed. Xie et al. (2001) reported that the HLCC is driven by the WSC dipole associated with this broad wake. However, the HLCC in their numerical model extended all the way to the Asian coast. Yu et al. (2003) analyzed the drifter data and concluded that the western edge of the HLCC is located around the International Date Line. They interpreted the shorter length of the HLCC was due to energy dissipation from the mean flow by mesoscale eddies. Kobashi and Kawamura (2002) investigated seasonal variations in the HLCC using hydrographic data, and pointed out that the HLCC is strong from summer to winter and becomes weak in spring. Sasaki et al. (2010) explored the mechanisms of seasonal variations using a numerical model, and concluded that the seasonal variations of the HLCC are induced by oceanic Rossby waves generated by the annual cycle of the trade winds.

Studies that focused on the interannual variations in the HLCC are very few. From analyses of satellite altimeter data, Sasaki et al. (2010) and Sasaki et al. (2012) reported that the HLCC was strong in 2003 and 2005. In these years, however, Sasaki et al. (2010) found that the satellite-derived wind stress was rather weak. Furthermore,

their numerical model driven by the high-resolution wind data failed to reproduce a strong HLCC in 2005. Sasaki et al. (2012) analyzed hydrographic data focusing on potential vorticity (PV), and concluded that low PV water advected from the north of the HLCC pushed the upper pycnocline upward and then enhanced the HLCC in these years. However, Sasaki et al. (2012) only showed results in these typical two years (2003 and 2005).

In this study, we explore the interannual variations in the HLCC. Spaceborne altimeter data over a period of 16 years enable us to capture spatiotemporal variations in the HLCC, and discuss the physical mechanisms for interannual variations. We also utilize a simple model to investigate the mechanisms further. The paper is organized as follows: section 2 describes the data used, section 3 discusses the features of the HLCC, section 4 describes the interannual variations of the HLCC, section 5 explores the possible mechanisms, and section 6 presents the summary.

2. Data

The along-track sea surface height anomaly (SSHA) data based on measurements by the TOPEX/Poseidon and Jason-1 altimeters for a period ranging from January 1993 to December 2008 were obtained from the Archiving, Validation, and Interpretation of Satellite Oceanographic (AVISO) data center. The SSHA was defined as an anomaly from the mean sea surface height over a period ranging from 1993 to 1999. The spatial resolution along the ground tracks is 5.8 km, and the temporal interval is 9.916 days. The SSHA was averaged in grid cells of $1/4^\circ \times 1/4^\circ$ over a month. The gridded monthly SSHA fields were spatially smoothed using a Gaussian filter with an e-folding scale of 100 km.

To estimate the absolute sea surface heights, a “quasi-absolute” mean sea surface height (*MSSH*) field was constructed by combining the altimeter SSHAs with the data obtained from Argo floats (Abe and Hanawa, 2010) according to the method proposed by Kuragano and Shibata (1997) and Uchida and Imawaki (2003). The real-time quality-controlled Argo data obtained from the Argo Global Data Assembly Center and further processed by Oka et al. (2007) were used. The dynamic SSH referenced to 1000 db, SSH_{Argo} , was calculated from temperature and salinity profiles measured by Argo floats, and collocated with the SSHA observations by altimeters, $SSHA_{ALT}$, allowing separations of 20 km in space and 2.5 days in time.

The *MSSH* at the collocated point is obtained as

$$MSSH = SSH_{Argo} - SSHA_{ALT}. \quad (1)$$

Since the $SSHA_{ALT}$ is an anomaly relative to the SSH averaged from 1993 to 1999, the *MSSH* computed from Eq. (1) is also the average over the seven years, even if SSH_{Argo} was obtained in 2000s. The number of collocated data points in a region from 15°N to 25°N and from 170°E to 150°W were 24,903. The *MSSH* was averaged in grid cells of $1/4^\circ \times 1/4^\circ$ and smoothed by a Gaussian filter with an e-folding scale of 100 km. The “quasi-absolute” sea surface height at a given point and time, *QASSH*, was estimated by

$$QASSH = MSSH + SSHA_{ALT}. \quad (2)$$

We also utilized the drifter data for a period ranging from 1993 to 1999, released from the Marine Environmental Data Service, Fisheries and Oceans Canada.

The drifter data were quality-controlled and gridded at temporal intervals of 6 h. Data from drifters equipped with a drogue centered at 15 m depth were selected to avoid downwind slip and high frequency noise. There were 74,010 data points in the region. The eastward velocity averaged in grid cells of $1/4^\circ \times 1/4^\circ$ was smoothed by a Gaussian filter with an e-folding scale of 100 km.

Two sets of sea surface wind stress data were used in this study. The first set is derived from measurements made by the SeaWinds scatterometer on the QuikSCAT satellite and produced by the National Oceanic and Atmospheric Administration (NOAA) Coastwatch Program. The spatial resolution is $1/8^\circ \times 1/8^\circ$, and the temporal interval is one day. The data period ranges from January 2000 to December 2008. The second set of data is a reanalysis product released by the National Center of Environmental Prediction/National Center for Atmospheric Research (NCEP/NCAR, Kalnay et al. 1996). The spatial grids of the NCEP/NCAR reanalysis are T63, which are approximately equal to $1.9^\circ \times 1.9^\circ$ (longitude \times latitude). The temporal interval is one month. The data period ranges from January 1949 to December 2009. The QuikSCAT wind stress product has a higher spatial resolution but covers a shorter period, whereas the NCEP/NCAR reanalysis covers a longer period with lower spatial resolution.

3. Climatology of the HLCC

Figure 1 shows climatological features of (a) the $QASSH$ and zonal geostrophic current velocity and (b) the temporal stability of the current field. An eastward current, the HLCC, is clearly exhibited to the west of the Hawaii Islands. The maximum eastward velocity reaches approximately 6 cm s^{-1} . To the west of the HLCC, several subtropical countercurrents (STCCs) are addressed. To the north and south of the HLCC,

strong eastward and westward velocities of the Kuroshio Extension and the NEC are discernible, respectively.

To assess robustness of the HLCC found in the climatological mean velocity field, the stability parameter (S) was calculated and is shown in Fig. 1(b). The value of S at a given point was defined as the ratio of the absolute value of the vector-mean velocity to the scalar-mean velocity:

$$S = \left| \frac{1}{N} \left(\sum_{t=1}^N \boldsymbol{v}(t) \right) \right| / \left(\frac{1}{N} \sum_{t=1}^N |\boldsymbol{v}(t)| \right), \quad (3)$$

where \boldsymbol{v} is the current vector, t is time, and N is the number of data. Fields of $QASSH$ calculated by Eq. (2) were utilized to compute the time series of the geostrophic velocity, $\boldsymbol{v}(t)$. If the value of S is close to 1 (0), the current system is stable (unstable) in time, implying that the signal of the mean velocity is dominant compared to velocity modulations including the eddy activities and meanderings of current.

Figure 1(b) shows that the NEC ($S \sim 0.9$) is a very stable current system. The Kuroshio Extension is relatively stable west of 155°E ($S > 0.6$), whereas it is unstable east of 155°E due to variations of the axis position (Qiu and Chen, 2005). The stability parameters in the HLCC (0.6 – 0.7), in which high eddy activities are reported (Yoshida et al. 2010; Yoshida et al. 2012), are smaller compared to those in the NEC and KE. However, these are slightly higher than those in the surrounding area, suggesting the eastward current in the HLCC is relatively stable.

Figure 2 shows (a) the zonal geostrophic current velocity calculated from the $MSSH$ in Eq. (1) averaged over a period ranging from 1993 to 1999 (Abe and Hanawa, 2010), (b) mean zonal current velocity estimated from the drifter data for the same period. In Fig. 2(a), a zonal band with a relatively strong eastward current up to 6–7 cm

s^{-1} , corresponding to the HLCC, is identified to the west of the Hawaii Islands. The eastward current extends to the west across the International Date Line. However, the stability parameter in Fig. 1(b) decreases significantly to the west of 170°W , implying that the signal of eastward velocity in the climatological mean field is ambiguous compared to the eddy activities in this region.

The zonal band of eastward velocity of the HLCC based on the drifter measurements in Fig. 2(b) is meridionally narrower than that calculated from the altimeter-derived *MSSH* in Fig. 2(a). A spatial filter utilized to fill the gaps between the altimeter ground tracks made the *MSSH* field in Fig. 2(a) smoother. The maximum eastward velocity reaches up to 11 cm s^{-1} , and the western edge of the HLCC is located at 173°W in Fig. 2(b). These features are consistent with results reported by Qiu et al. (1997).

4. Interannual variations in the HLCC

Figure 3 shows the annual mean *QASSH* and zonal geostrophic velocity during a period ranging from 1993 to 2008. Significant interannual variations in the intensity and location of the HLCC are discernible. While the eastward velocity of the HLCC was weak in 2000, it extended to and beyond the International Date Line in 2003 and 2005, as Sasaki et al. (2012) reported.

To explore the interannual variations quantitatively, we set a box extending from 173°W to 157°W and 16.5°N to 22.5°N (Figs. 2 and 3), which covers the north-south limits of the annual mean HLCC locations. In the box, the zonal velocity component was averaged zonally in meridional bins of $1/4^{\circ}$. Meridional location of the HLCC axis was determined by choosing the maximum zonally averaged zonal velocity.

Figure 4 shows time series of (a) the zonal velocity at the HLCC axis, and (b) the latitude of the axis. The averages of the maximum zonal velocity and latitude of the axis over the period ranging from 1993 to 2008 were 5.5 cm s^{-1} and 19.8°N , and the standard deviations were 2.6 cm s^{-1} and 1.2° , respectively.

Figure 5 shows frequency distributions and annual means of (a) the zonal velocity at the HLCC axis and (b) the meridional axis locations, computed from the data shown in Fig. 4. The HLCC was strong in 1994, 1999, and from 2001 to 2005, and it was very weak in 2000, as shown in the maps of zonal velocity in Fig. 3. The annual means of the zonal velocity at the HLCC axis in Fig. 5(a) are not correlated with the locations of the axis in Fig. 5 (b) (correlation coefficient $r = -0.02$). However, the standard deviation of the axis latitude is opposite in phase with the annual mean zonal velocity of the HLCC. As shown in Fig. 6, time series of eastward velocity and the standard deviation of the axis location are negatively correlated ($r = -0.61$), indicating that the HLCC is stronger when the location of the axis is stable. This correlation coefficient exceeds a significance level of 10%, when the degree of freedom (DOF) is assumed to be 8. In this study, the DOF is defined by number of peaks counted subjectively from the two time series.

5. Possible mechanisms for the interannual variations

5.1 Wind forcing

Figure 7 shows (a) a map of the WSC calculated from the QuikSCAT wind data, averaged over a period ranging from 2000 to 2008, (b) the WSC spatially filtered by a Gaussian filter with an e-folding scale of $3^\circ \times 1^\circ$, (c) latitude-time diagram of

meridional gradient anomaly of the WSC, averaged zonally from 173°W to 157°W, and (d) time series of the gradient anomaly, averaged meridionally from 18°N to 21°N. The time series were smoothed by a 13-month running mean filter in time. Orographic dipoles formed in the lee of the islands (Fig. 7(a)), sustained by the northeasterly trade wind, are found. Spatial smoothing in the field combines the WSCs, and a broad dipole emerges (Fig. 7(b)).

Since the negative (positive) WSC causes convergence (divergence) of Ekman current, the WSC dipole makes the SSH low toward the north, hence eastward geostrophic current is generated. This broad WSC dipole is the driving force of the formation (Xie et al., 2001) and seasonal variation (Sasaki et al., 2010) of the HLCC. Positive anomaly in the meridional gradient of the WSC toward the north corresponds to strengthening of the dipole. In the latitude of the HLCC (approximately 18°N – 21°N), the gradient anomaly is positive in 2001 – 2002 and 2007 – 2008, and negative in 2004 – 2005 (Fig. 7(c)). This result is in good agreement with that of Sasaki et al. (2012). However, the correlation between the meridional gradient of the WSC and the zonal geostrophic velocity in the HLCC is negative ($r = -0.81$, exceeding a significance level of 10% (DOF = 3), Fig. 7(d)), suggesting that the WSC dipole cannot explain the interannual variations in the HLCC velocity.

Note that the meridional gradient of the WSC is proportional to an acceleration of the zonal velocity. To be exact, the zonal velocity (not the acceleration) is not appropriate to be compared with the WSC gradient as in Fig. 7(d). To show that, a hindcast model (1.5 layer, reduced gravity model) was utilized following Qiu (2003). Under the long-wave approximation, the linear vorticity equation is obtained as follows:

$$\frac{\partial h}{\partial t} - C_R \frac{\partial h}{\partial x} = - \frac{g' \mathbf{k} \cdot \nabla \times \boldsymbol{\tau}}{\rho_0 g f}, \quad (4)$$

where h is the SSHA to be obtained, $\boldsymbol{\tau}$ is the wind stress vector, C_R is the speed of the long baroclinic Rossby waves, g' is the reduced gravity, ρ_0 is the reference density, f is the Coriolis parameter, and \mathbf{k} is the unit vector in the vertical direction. For simplicity, factors other than h and $\boldsymbol{\tau}$ are assumed to be constant in time and space. Taking meridional derivative of Eq. (4) and assuming the geostrophic balance

$$fu = -g \frac{\partial h}{\partial y}, \quad (5)$$

we obtain

$$\left(\frac{\partial}{\partial t} - C_R \frac{\partial}{\partial x} \right) u = \frac{g'}{\rho_0 f^2} \frac{\partial (\mathbf{k} \cdot \nabla \times \boldsymbol{\tau})}{\partial y}, \quad (6)$$

where u is the zonal velocity.

According to Eq. (6), the meridional gradient of the WSC (right hand side) is proportional to the acceleration of the zonal velocity along the westward propagation of the Rossby waves (left hand side). For this reason, the comparison of the two time series in Fig. 7(d) is not considered to be exact. However, the time scale of the smoothed WSC gradient in Fig. 7(d) (approximately 7 years) is much longer than transition time of the baroclinic Rossby waves propagating from the WSC dipole to the HLCC, which was estimated to be several months by Sasaki et al. (2010). Therefore, the forcing can be regarded as mostly constant during the propagation. Because the propagation time also can be assumed to be constant, the meridional gradient of the WSC is proportional to not only the acceleration of the zonal velocity but also to the velocity.

Although Sasaki et al. (2012) suggested the possibility that eastern part of the

HLCC close to the Hawaii Islands ($165^{\circ}\text{W} - 160^{\circ}\text{W}$) can be influenced by the orographic WSC dipole, the HLCC averaged in the box region ($173^{\circ}\text{W} - 157^{\circ}\text{W}$) is obviously out of phase with the meridional WSC gradient. This inconsistency implies that the interannual variations in the WSC dipole are not the dominant mechanism driving the interannual variations in the HLCC.

5.2 SSHA propagating from the east

Figure 8 shows longitude-time diagrams of the SSHA, averaged meridionally (a) from 17°N to 19°N and (b) from 20°N to 22°N , (c) the meridional difference of the SSHAs ((a) minus (b)), and (d) time series of the SSHA difference averaged zonally from 173°W to 157°W and eastward velocity at the HLCC axis. The SSHA fields and time series were smoothed by a Gaussian filter with an e-folding scale of 300 km in space and a 13-month running mean filter in time. Westward propagations of the SSHA are discernible on both northern and southern sides of the HLCC. The difference between the SSHAs may cause variations in the strength of the HLCC. Positive (negative) difference enhances (reduces) eastward velocity of the HLCC.

The time series in Fig. 8(d) clearly exhibits a strong correlation between the meridional SSHA difference and eastward velocity of the HLCC ($r = 0.87$, exceeding a significance level of 1% (DOF = 8)). The amplitude of 8 cm in the SSHA difference (2004 minus 2000) approximately corresponds to 5 cm s^{-1} in the zonal geostrophic velocity, which is comparable to the amplitude of 6.5 cm s^{-1} in the observed velocity variations. These results indicate that the interannual variations in the HLCC can be caused by the meridional gradient of the SSHA.

Figure 9 shows lag correlation coefficients between the SSHA difference in Fig.

8(c) and the HLCC velocity in Fig. 8(d), as a function of longitude. Positive correlations extending from the HLCC region can be traced back far east beyond the Hawaii Islands. This result confirms propagating SSHAs are originated in the area east of the Hawaii Islands.

To explore generation of the wind-driven SSHAs in the east of the Hawaii Islands, and examine relationships with the velocity variations in the HLCC, the hindcast model (Eq. (4)) was used according to Qiu (2003). By integrating Eq. (4) from the eastern boundary (x_e) along the baroclinic Rossby wave characteristic, we obtain

$$h(x, y, t) = h\left(x_e, y, t + \frac{x - x_e}{C_R}\right) + \frac{g'}{\rho_0 g f C_R} \int_{x_e}^x k \cdot \nabla \times \tau\left(x', y, t + \frac{x - x'}{C_R}\right) dx' \quad (7)$$

To calculate the $h(x, y, t)$ fields, the monthly averaged wind stress of the NCEP/NCAR reanalysis product was used. Plausible C_R was estimated from the observed SSHA on a longitude-time diagram as a function of latitude (not shown, $C_R = 16 \text{ cm s}^{-1}$ at 18°N and 10 cm s^{-1} at 21°N). The value of g' was set to 0.03 m s^{-2} . Along the eastern boundary, $h(x, y, t) = 0$ was assumed. The SSHAs were calculated at T63 grids (approximately $1.9^\circ \times 1.9^\circ$) of the NCEP/NCAR reanalysis product. The calculated SSHA was linearly interpolated to $1^\circ \times 1^\circ$ grids.

Figure 10 shows longitude-time diagrams and time series of the SSHA calculated by the hindcast model. Major patterns of the observed SSHA shown in Fig. 8 were reproduced on the (a) southern and (b) northern sides of the HLCC. The meridional difference of the SSHA calculated by the model (Fig. 10(c)) is also consistent with that of the observed SSHA (Fig. 8(c)). The time series in Fig. 10(d) confirms high correlation between the meridional SSHA difference and the strength of the HLCC deduced from the altimeter observations ($r = 0.56$, exceeding a significance

level of 10% (DOF = 8)). This modeled SSHA difference can also be traced back far east of the Hawaii Islands along positive correlation with the HLCC velocity (Fig. 11). The wind stress field to the east of the Hawaii Islands excites the SSHA, and the meridional gradient of the propagating SSHA generates the interannual variations in the strength of the HLCC.

Sasaki et al. (2012) proposed that advection of low PV water to the north of the HLCC could be a possible mechanism for the interannual variations in the HLCC. As they pointed out, the HLCC west of 170°W was strong in 2003 and 2005 (Fig. 3), when the low PV water was advected to this area. The results of the present study proposed a possibility that the WSC fields in the east of the Hawaii Islands can excite SSHA and cause the interannual variations in the HLCC in addition to the mechanism proposed by Sasaki et al. (2012). In the present study, we may not evaluate the contributions of these two mechanisms. Further studies using a realistic numerical model focused on this point are needed.

5.3 Wind stress field in the east

Figure 12 shows annual mean wind stress (arrows) and WSC (color) in (a) 1993, (b) 1999, (c) the difference ((b) minus (a)), and (d) the meridional gradient of (c). Since the meridional difference of the modeled SSHA was largest in 1994 and smallest in 2000 (Fig. 10), and the propagation of the SSHA from 140°W to the HLCC region takes approximately one year (Fig. 11), the wind stress and WSC fields in 1993 and 1999 were selected for comparison. In these years, negative and positive WSCs, formed by the northeasterly trade winds, were dominant in this region. The WSCs in 1993 were weak under weak trade winds, and strong in 1999 under the strong wind condition (Fig.

12(c)).

Since the position of the WSCs located between 140°W and 120°W is meridionally opposite to that in the lee of the Hawaii Islands (Fig. 12), the WSCs in the east of the Hawaii Islands generate westward flow along meridional boundary between the positive and negative WSCs (or negative meridional gradient of WSC difference in Fig. 12(d)). Because the HLCC is an eastward flow, strong (weak) WSCs in the east area weaken (strengthen) the HLCC with a time lag. The HLCC is strengthened (weakened) in 1994 (2000) one year after the emergence of weak (strong) WSCs in 1993 (1999), corresponding to the strong HLCC in 1994 and weak HLCC in 2000.

6. Summary

Interannual variations in the HLCC were investigated by analyzing 16 years of satellite altimeter data together with data from Argo floats and drifting buoys. Strong interannual variations were discernible in the zonal velocity at the HLCC axis and meridional axis location. The HLCC was stronger when the axis position was stable. The eastward velocity of the HLCC did not exhibit correlation with the strength of the WSC dipole, which are located on the leeward side of the Hawaii Islands, and considered to dominate the generation and seasonal variations in the HLCC.

Instead of the effects of the orographic WSC dipoles, we proposed a new mechanism for the generation of the interannual variations in the HLCC. The SSHA propagating westward from the east of the Hawaii Islands caused the interannual variations in the meridional gradient of the SSHA across the HLCC, resulting in the interannual variations in the eastward current of the HLCC. A simple linear baroclinic Rossby wave model with the NCEP/NCAR wind fields successfully reproduced this

process. The westward propagating SSHAs, which cause the interannual variations in the HLCC, were generated by the wind stress field to the east of the Hawaii Islands. The positive/negative WSCs in the east of the islands were formed by the trade wind, and excited the SSHAs in the region between the two WSCs. The SSHAs propagating westward caused the velocity variations in the HLCC with a time lag of one year.

Acknowledgments

We would like to thank the editor (Dr. Tomoki Tozuka), the reviewer (Dr. Hideharu Sasaki) and an anonymous reviewer, who helped improve the manuscript. We are grateful to the members of the Physical Oceanography Laboratory in Tohoku University for their fruitful discussions and valuable comments. This work was partly supported by the Sasagawa Scientific Research Grant, and the Global Center of Excellence Program, “Global Education and Research Center for Earth and Planetary Dynamics,” promoted by the Tohoku University. Dr. Eitarou Oka kindly provided the quality-controlled Argo float data. The altimeter data product was provided by the AVISO, the drifting buoy data by Marine Environmental Data Service, the surface wind stress data by the NOAA Coast Watch and NCEP/NCAR. We would like to thank all the data providers.

References

- Abe, H., and K. Hanawa, 2010: "Mean sea surface height in the world ocean using Argo float and altimetry" in Proceedings of OceanObs'09: Sustained Ocean Observations and Information for Society (Annex), Venice, Italy, 21-25 September 2009, Hall, J., Harrison, D.E. & Stammer, D., Eds., ESA Publication WPP-306.
- Flament, P., S. Kennan, R. Lumpkin, M. Sawyer, and E. Stroup, 1998: The ocean. *Atlas of Hawaii*, S. P. Juvik, and J. O. Juvik, 3d Ed., Univ. of Hawaii Press, Honolulu, 82-86.
- Kalnay, E., and coauthors, 1996: The NCEP/NCAR 40-year reanalysis project. *Bull. Amer. Meteor. Soc.*, **77**, 437-471.
- Kobashi, F., and H. Kawamura, 2002: Seasonal variation and instability nature of the North Pacific Subtropical Countercurrent and the Hawaiian Lee Countercurrent. *J. Geophys. Res.*, **107**(C11), 3185, doi:10.1029/2001JC001225.
- Kuragano, T., and A. Shibata, 1997: Sea surface dynamic height of the Pacific Ocean derived from TOPEX/POSEIDON altimeter data: Calculation method and accuracy. *J. Oceanogr.*, **53**, 585-599.
- Oka, E., L. D. Talley and T. Suga, 2007: Temporal variability of winter mixed layer in the mid-to high-latitude North Pacific. *J. Oceanogr.*, **63**, 293-307.
- Qiu, B., D. Koh, C. Lumpkin, and P. Flament, 1997: Existence and formation mechanism of the North Hawaiian Ridge Current. *J. Phys. Oceanogr.*, **27**, 431-444.
- Qiu, B., 2003: Kuroshio Extension variability and forcing of the Pacific decadal oscillations: Responses and potential feedback. *J. Phys. Oceanogr.*, **33**, 2465-2482.
- Qiu, B., and S. Chen, 2005: Variability of the Kuroshio Extension jet, recirculation gyre,

and mesoscale eddies on decadal time scales. *J. Phys. Oceanogr.*, **35**, 2090-2103.

Sasaki, N., S. P. Xie, B. Taguchi, M. Nonaka, and Y. Masumoto, 2010: Seasonal variations of the Hawaiian Lee Countercurrent induced by the meridional migration of the trade winds. *Ocean Dynamics*, **60**, 705-715, doi:10.1007/s10236-009-0258-6.

Sasaki, H., S.-P. Xie, B. Taguchi, M. Nonaka, S. Hosoda, and Y. Masumoto, 2012: Interannual variations of the Hawaiian Lee Countercurrent induced by potential vorticity variability in the subsurface. *J. Oceanogr.*, **68**, 93-111, doi:10.1007/s10872-011-0074-8.

Uchida, H., and S. Imawaki, 2003: Eulerian mean surface velocity field derived by combining drifter and satellite altimeter data. *Geophys. Res. Lett.*, **30**, 1229, doi:10.1029/2002GL016445.

Xie, S. P., W. T. Liu, and M. Nonaka, 2001: Far-reaching effects of the Hawaiian Islands on the Pacific ocean-atmosphere system. *Science*, **292**, 2057–2060, doi:10.1126/science.1059781.

Yoshida, S., B. Qiu, and P. Hacker, 2010: Wind-generated eddy characteristics in the lee of the island of Hawaii. *J. Geophys. Res.*, **115**, C03019, doi:10.1029/2009JC005417.

Yoshida, S., B. Qiu, and P. Hacker, 2011: Low-frequency eddy modulations in the Hawaiian Lee Countercurrent: Observations and connection to the Pacific Decadal Oscillation. *J. Geophys. Res.*, **116**, C12009, doi:10.1029/2011JC007286.

Yu, Z., N. Maximenko, S. P. Xie, and M. Nonaka, 2003: On the termination of the Hawaiian Lee Countercurrent. *Geophys. Res. Lett.*, **30**(5), 1215, doi:10.1029/2002

419 GL016710.

420

Figure captions

Figure 1: (a) Eastward geostrophic current (color, cm s^{-1}) and (b) stability parameter (S , color) estimated from *QASSH* using Eq. (3) with the *QASSH* averaged over the period from 1993 to 2008 (contours, cm). Regions where numbers of altimeter data points collocated with Argo profiles are insufficient are masked.

Figure 2: (a) Zonal geostrophic current velocity calculated from the *MSSH* as an average over a period ranging from 1993 to 1999 (Abe and Hanawa, 2010), (b) mean zonal current velocity estimated from the drifter data for the same period.

Figure 3: Annual mean zonal velocity (shading) and *QASSH* (contours, 5 cm interval). The velocity and *QASSH* averaged over the 16 years are also shown in the last panel.

Figure 4: Time series of the monthly mean (a) zonal velocity at the axis of the HLCC, and (b) latitude of the HLCC axis.

Figure 5: Frequency distribution of the monthly mean (a) zonal velocity at the HLCC axis, and (b) latitude of the HLCC axis (horizontal bars). The averages and standard deviations computed each year are shown by thick lines and vertical bars, respectively.

Figure 6: Annual mean zonal velocity at the HLCC axis shown in Fig. 5(a) (solid line, left axis), and standard deviation of the latitude of the HLCC axis shown in Fig. 5(b) (dashed line, right axis).

Figure 7: (a) The WSCs averaged over a period ranging from 2000 to 2008, estimated using the NOAA Coastwatch QuikSCAT wind stress product, (b) same as (a) but spatially filtered WSCs using a Gaussian filter with an e-folding scale of $3^\circ \times 1^\circ$, (c) latitude-time diagram of meridional gradient anomaly of the WSC averaged zonally from 173°W to 157°W , and (d) time series of the gradient anomalies averaged meridionally from 18°N to 21°N (solid line, left axis) and zonal velocity of the HLCC calculated from the time series in Fig. 4(a) (dashed line, right axis).

Figure 8: Longitude-time diagrams of the SSHA averaged meridionally (a) from 17°N to 19°N and (b) from 20°N to 22°N , (c) the meridional difference of the SSHA ((a) minus (b)), and (d) time series of the SSHA difference averaged zonally from 173°W to 157°W (solid line, left axis) and the zonal velocity at the HLCC axis calculated from the time series in Fig. 4(a) (dashed line, right axis).

Figure 9: Lag correlation coefficients between the meridional difference of the observed SSHA in Fig. 8(c) and the HLCC velocity in Fig. 8(d), as a function of longitude. Positive lag means that the SSHA difference leads the velocity. The coefficients exceeding a significance level of 10 % ($r > 0.55$, $\text{DOF} = 8$) are denoted by black dots.

Figure 10: Same as that in Fig. 9 but using the SSHA calculated by the linear baroclinic Rossby wave model and the wind data from the NCEP/NCAR reanalysis.

Figure 11: Lag correlation coefficients between the meridional difference of the

modeled SSHA in Fig. 10(c) and the HLCC velocity in Fig. 10(d), as a function of longitude. Positive lag means that the SSHA difference leads the velocity. The coefficients exceeding a significance level of 10 % ($r > 0.55$, $\text{DOF} = 8$) are denoted by black dots.

Figure 12: A map of annual mean wind stress vector (arrows), WSC (color) in (a) 1993, (b) 1999, (c) the difference of the WSC ((b) minus (a)), and (d) meridional gradient of (c), calculated from the wind data from the NCEP/NCAR reanalysis.

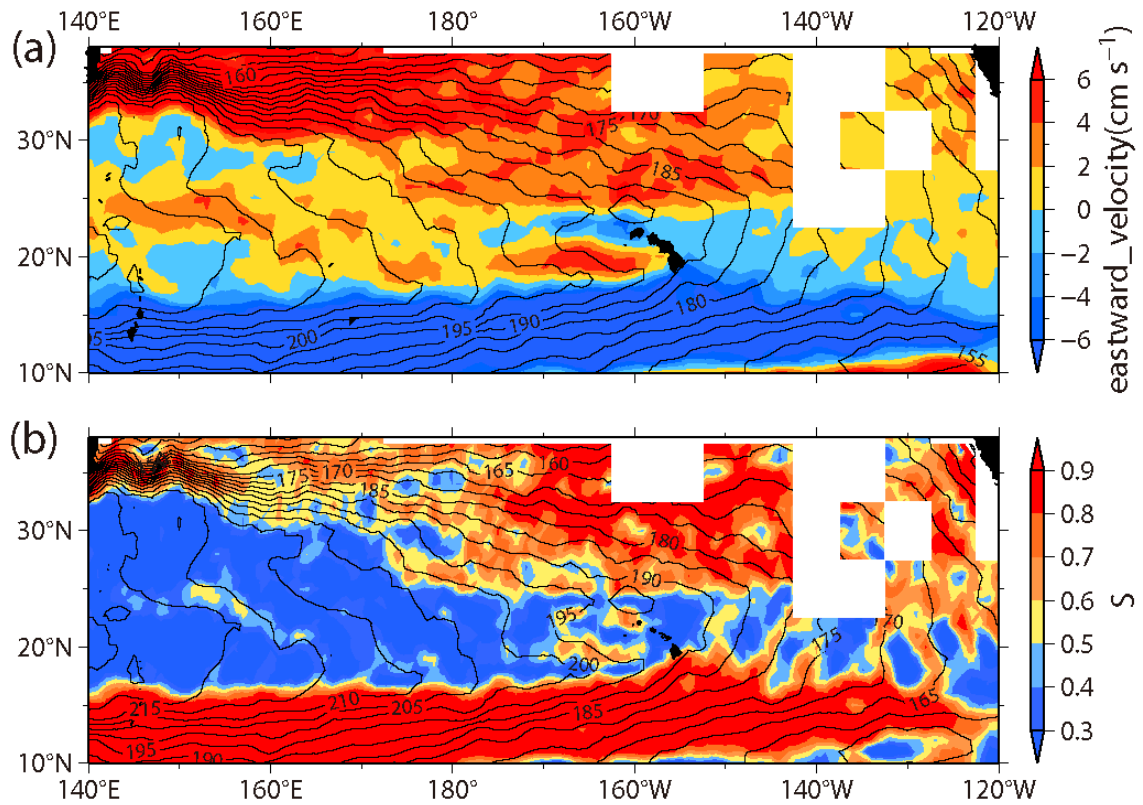


Figure 1: (a) Eastward geostrophic current (color, cm s^{-1}) and (b) stability parameter (S , color) estimated from *QASSH* using Eq. (3) with the *QASSH* averaged over the period from 1993 to 2008 (contours, cm). Regions where numbers of altimeter data points collocated with Argo profiles are insufficient are masked.

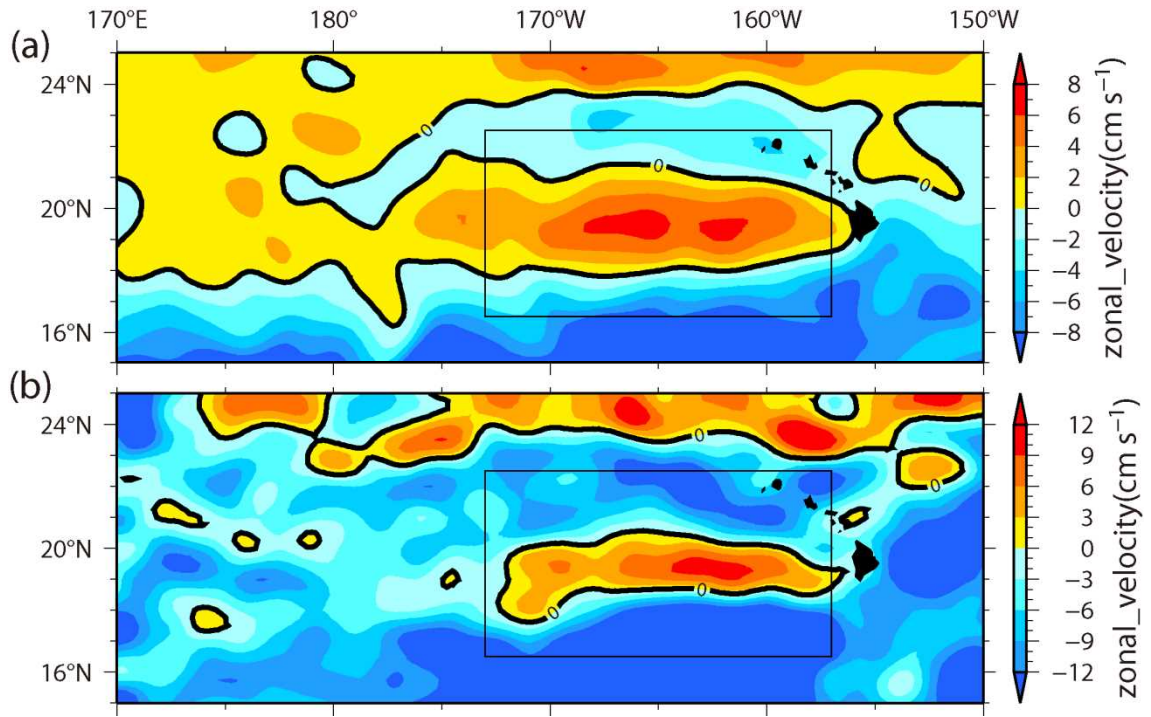


Figure 2: (a) Zonal geostrophic current velocity calculated from the *MSSH* as an average over a period ranging from 1993 to 1999 (Abe and Hanawa, 2010), (b) mean zonal current velocity estimated from the drifter data for the same period.

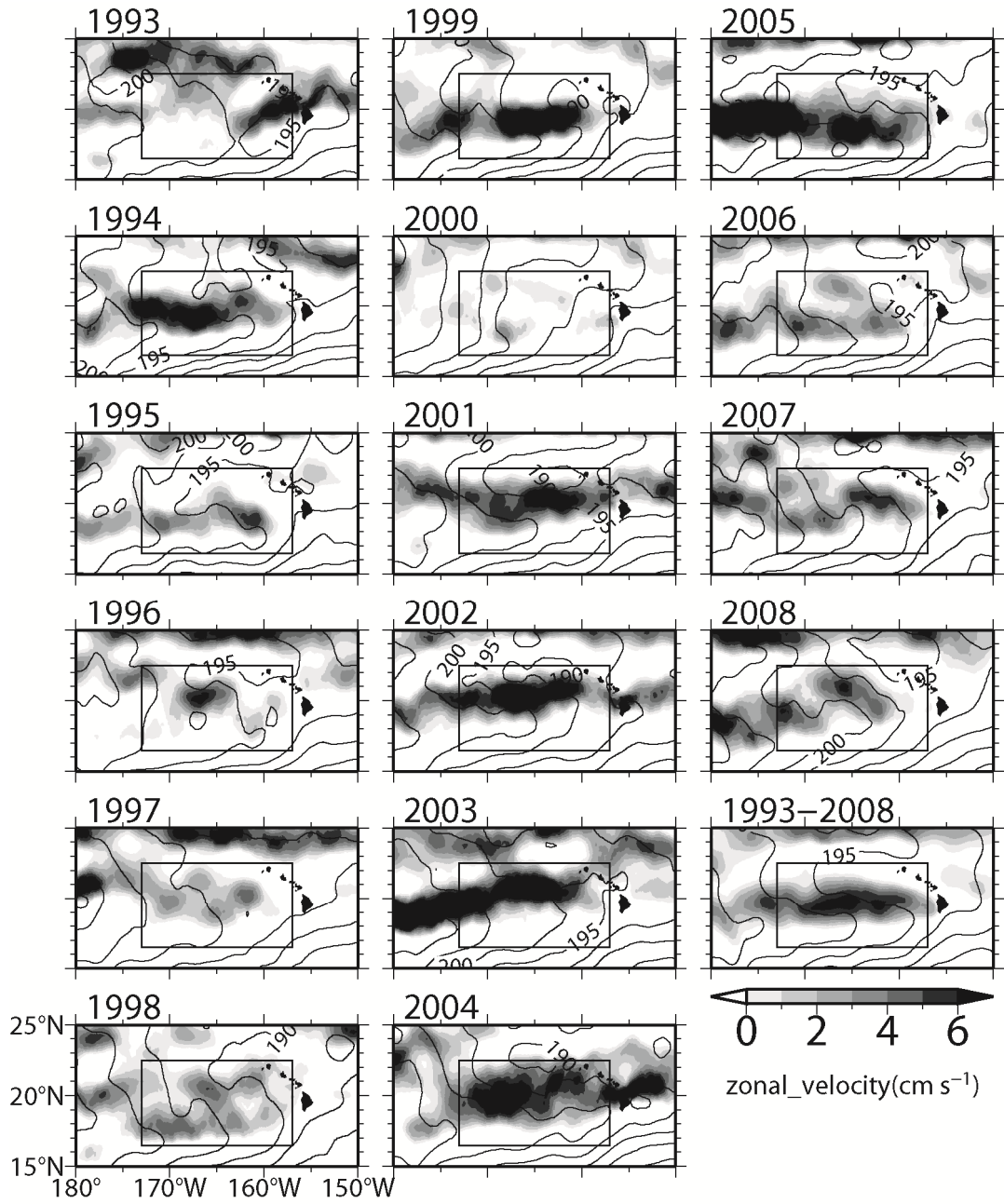


Figure 3: Annual mean zonal velocity (shading) and $QASSH$ (contours, 5 cm interval). The velocity and $QASSH$ averaged over the 16 years are also shown in the last panel.

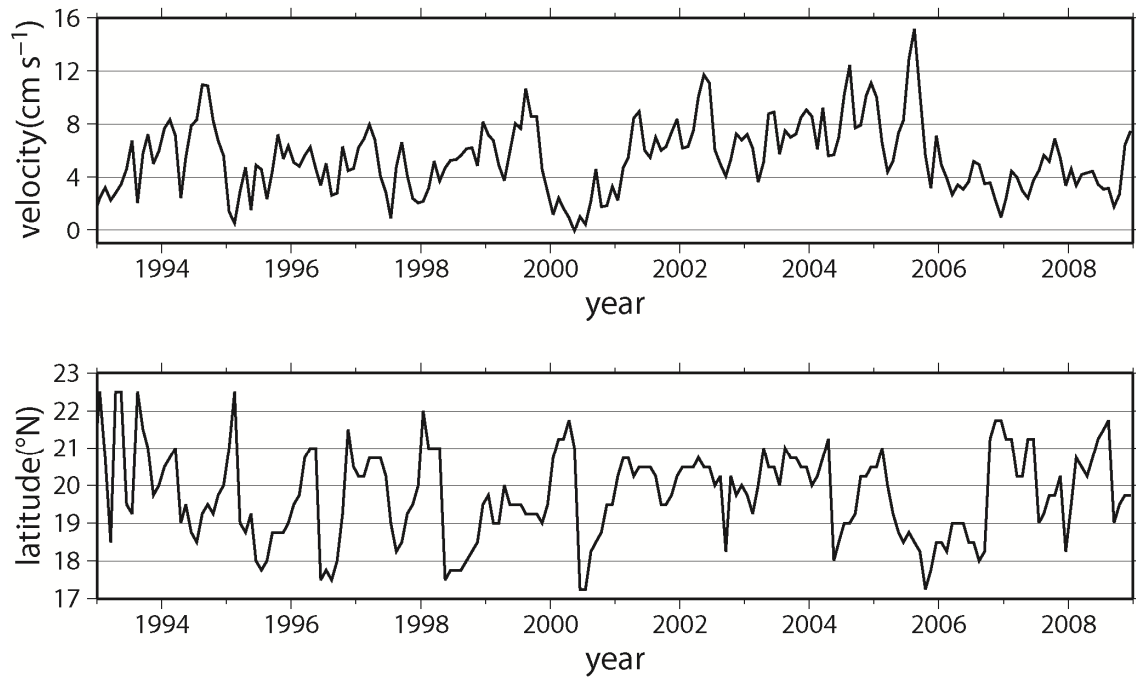


Figure 4: Time series of the monthly mean (a) zonal velocity at the axis of the HLCC, and (b) latitude of the HLCC axis.

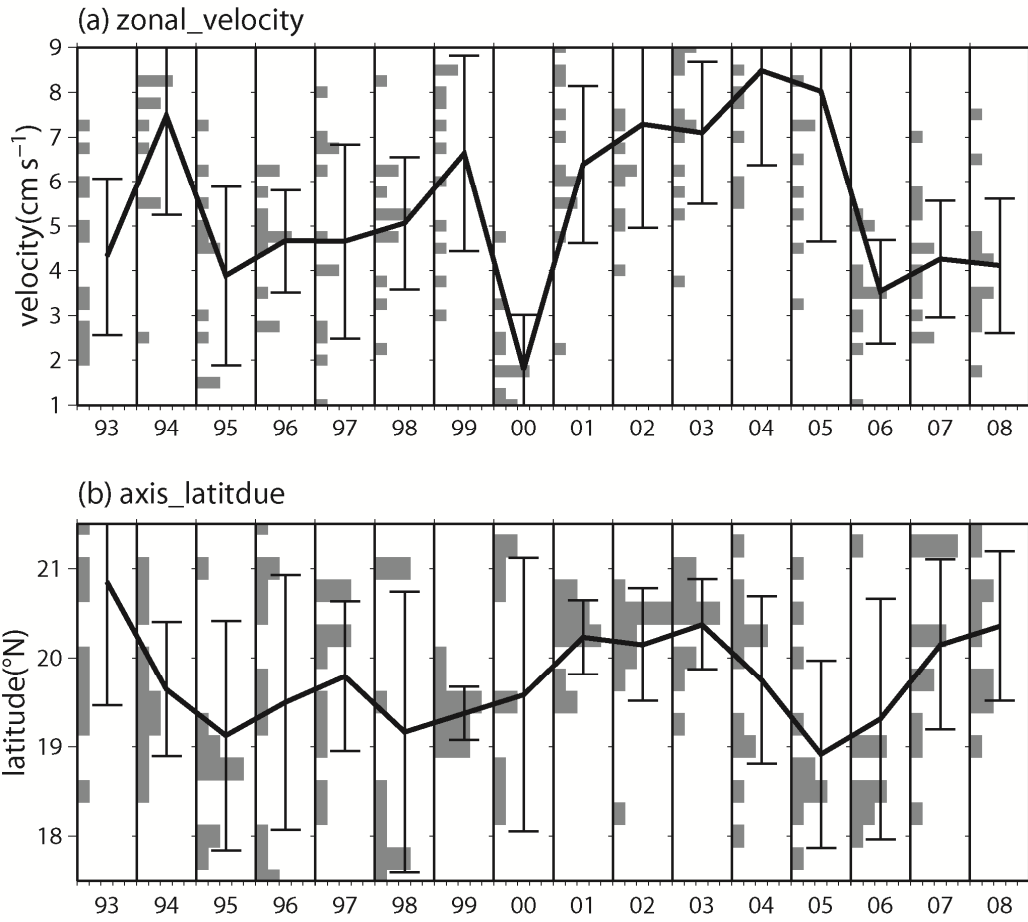


Figure 5: Frequency distribution of the monthly mean (a) zonal velocity at the HLCC axis, and (b) latitude of the HLCC axis (horizontal bars). The averages and standard deviations computed each year are shown by thick lines and vertical bars, respectively.

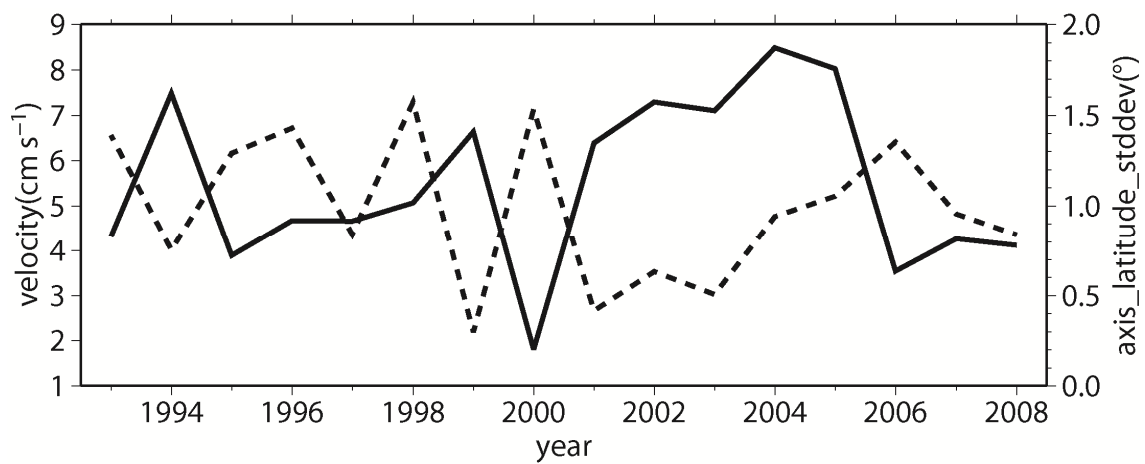


Figure 6: Annual mean zonal velocity at the HLCC axis shown in Fig. 5(a) (solid line, left axis), and standard deviation of the latitude of the HLCC axis shown in Fig. 5(b) (dashed line, right axis).

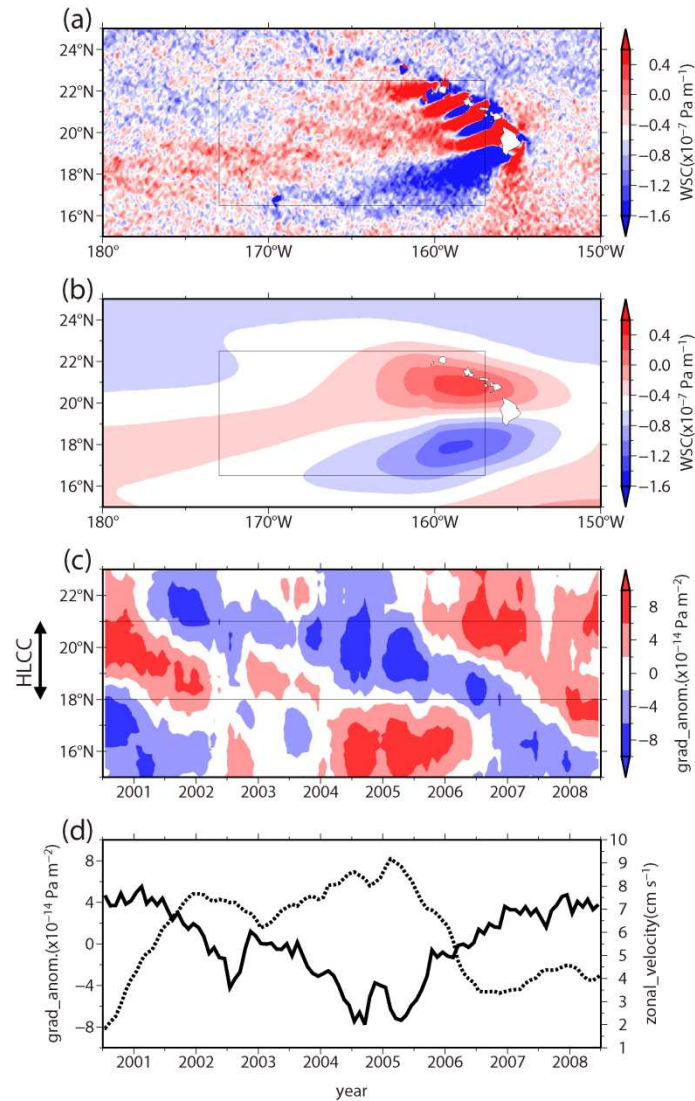


Figure 7: (a) The WSCs averaged over a period ranging from 2000 to 2008, estimated using the NOAA Coastwatch QuikSCAT wind stress product, (b) same as (a) but spatially filtered WSCs using a Gaussian filter with an e-folding scale of $3^\circ \times 1^\circ$, (c) latitude-time diagram of meridional gradient anomaly of the WSC averaged zonally from 173°W to 157°W , and (d) time series of the gradient anomalies averaged meridionally from 18°N to 21°N (solid line, left axis) and zonal velocity of the HLCC calculated from the time series in Fig. 4(a) (dashed line, right axis).

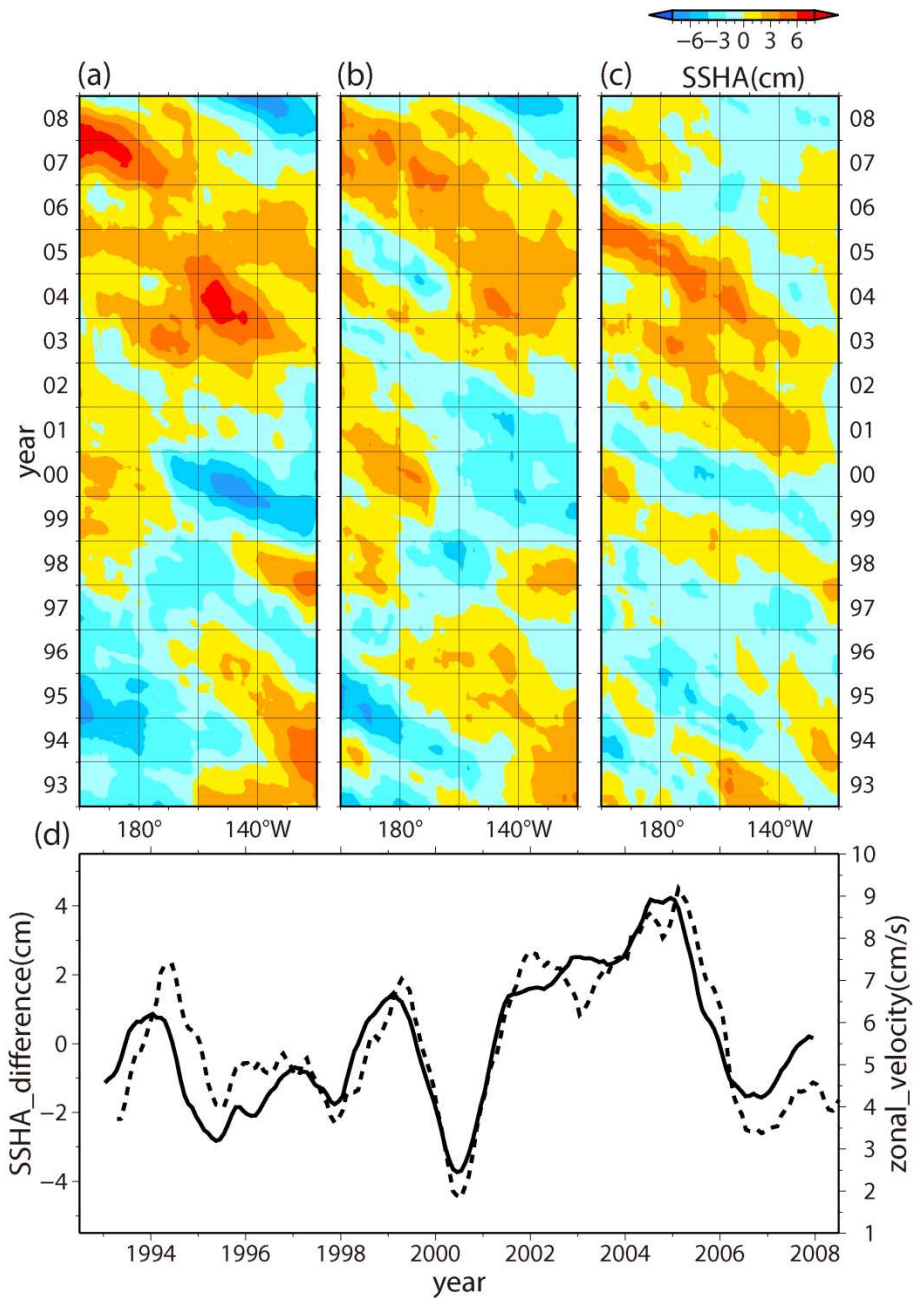


Figure 8: Longitude-time diagrams of the SSHA averaged meridionally (a) from 17°N to 19°N and (b) from 20°N to 22°N, (c) the meridional difference of the SSHA ((a) minus (b)), and (d) time series of the SSHA difference averaged zonally from 173°W to 157°W (solid line, left axis) and the zonal velocity at the HLCC axis calculated from the time series in Fig. 4(a) (dashed line, right axis).

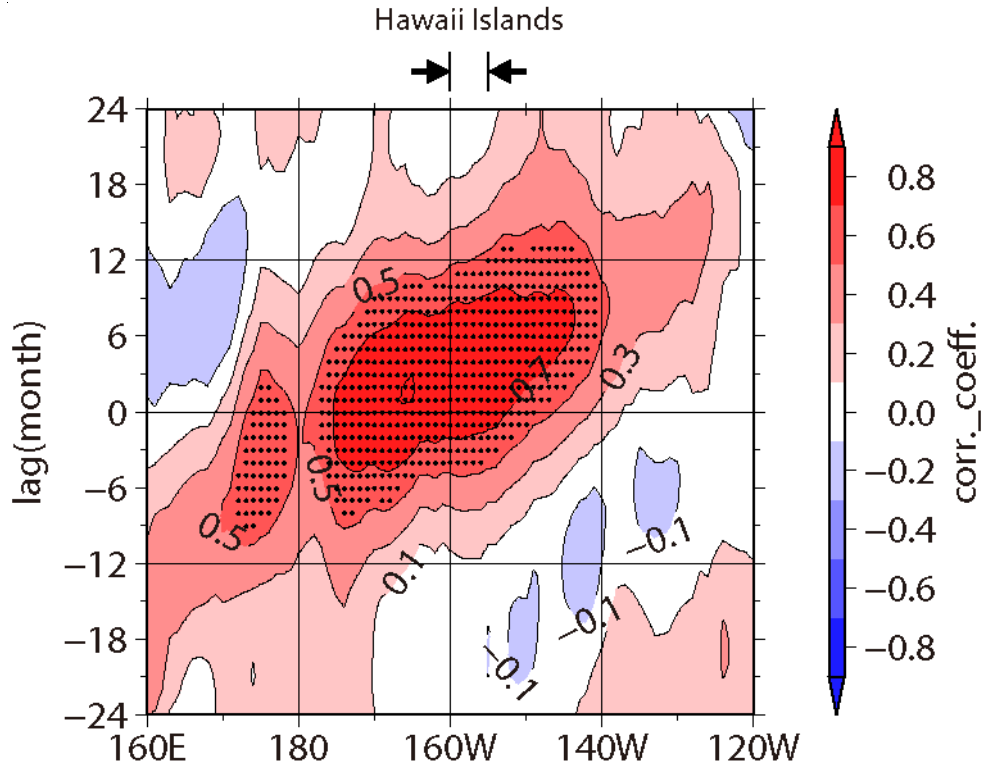


Figure 9: Lag correlation coefficients between the meridional difference of the observed SSHA in Fig. 8(c) and the HLCC velocity in Fig. 8(d), as a function of longitude. Positive lag means that the SSHA difference leads the velocity. The coefficients exceeding a significance level of 10 % ($r > 0.55$, $\text{DOF} = 8$) are denoted by black dots.

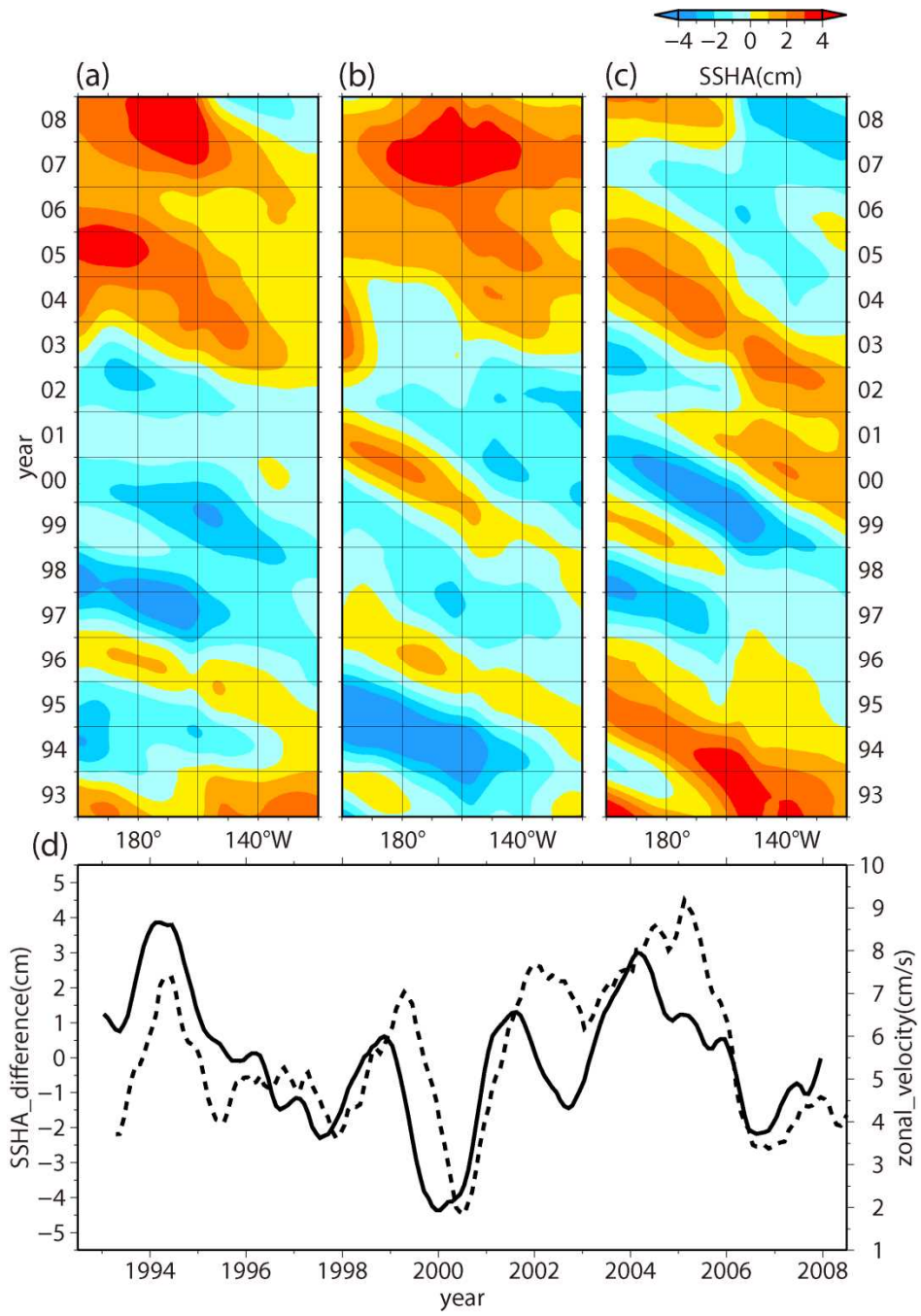


Figure 10: Same as that in Fig. 9 but using the SSHA calculated by the linear baroclinic Rossby wave model and the wind data from the NCEP/NCAR reanalysis.

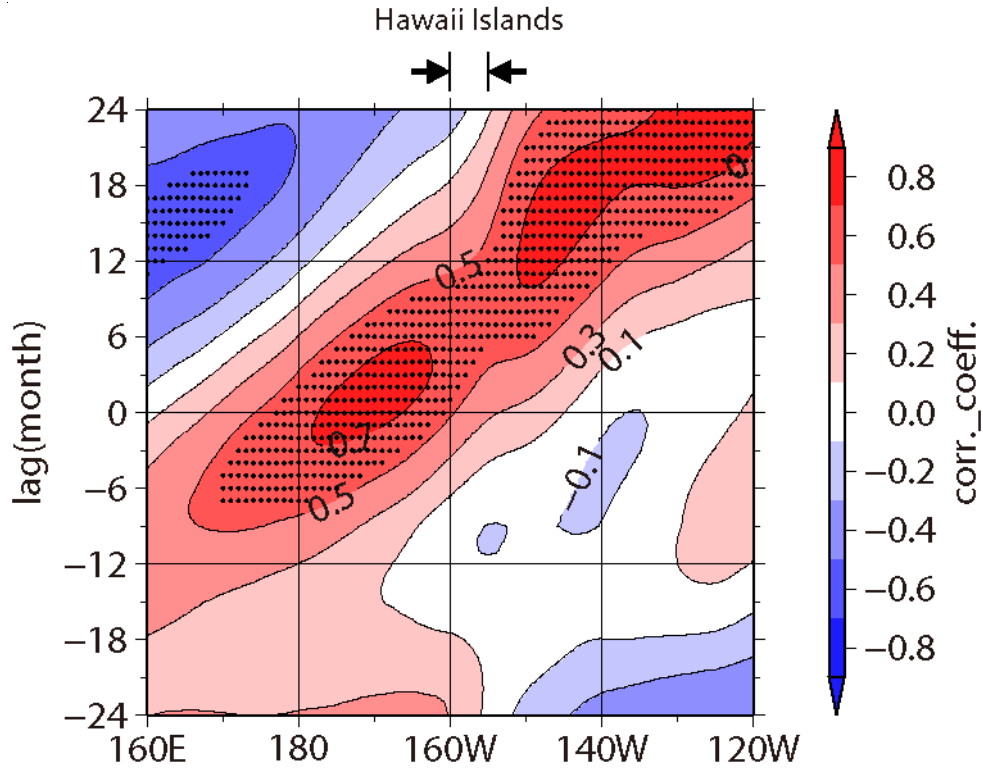


Figure 11: Lag correlation coefficients between the meridional difference of the modeled SSHA in Fig. 10(c) and the HLCC velocity in Fig. 10(d), as a function of longitude. Positive lag means that the SSHA difference leads the velocity. The coefficients exceeding a significance level of 10 % ($r > 0.55$, $DOF = 8$) are denoted by black dots.

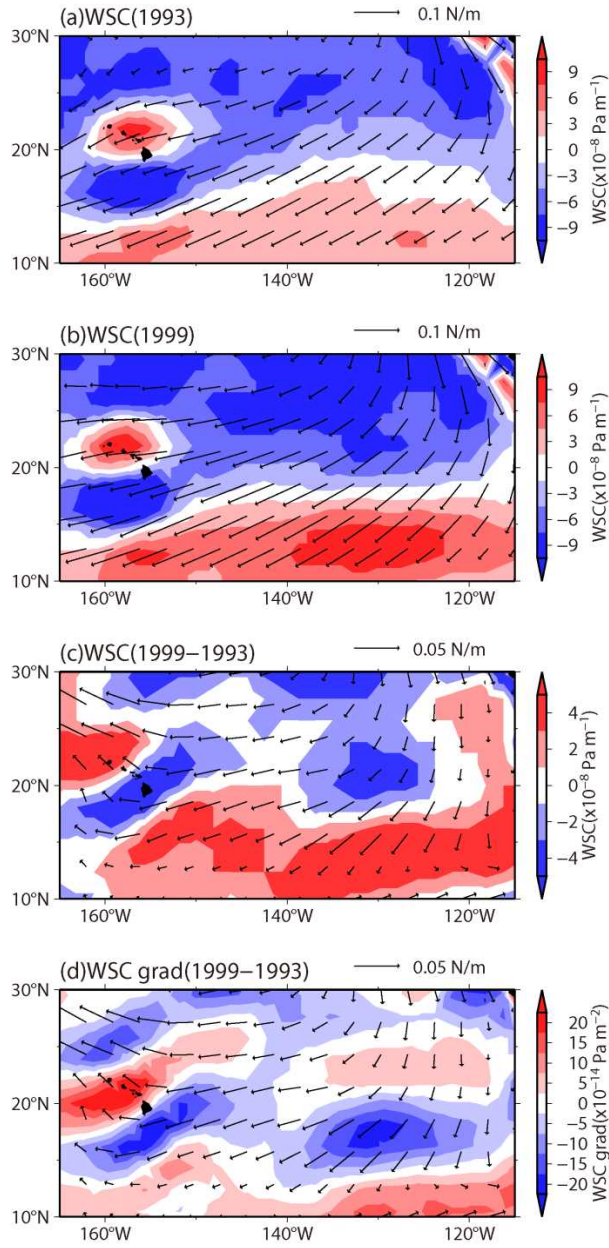


Figure 12: A map of annual mean wind stress vector (arrows), WSC (color) in (a) 1993, (b) 1999, (c) the difference of the WSC ((b) minus (a)), and (d) meridional gradient of (c), calculated from the wind data from the NCEP/NCAR reanalysis.